INTRODUCING THE GLOBAL MAPPING OF FLOOD DYNAMICS USING GNSS-REFLECTOMETRY AND THE CYGNSS MISSION

Pierre Zeiger[1,*], Frédéric Frappart[2], José Darrozes[3]

[1]Laboratoire d'Etudes en Géophysique et Océanographie Spatiale (LEGOS), Université Paul Sabatier (UPS), Toulouse, France
[2]Interaction Sol Plante Atmosphère (ISPA), INRAE Bordeaux, Villenave-d'Ornon, France
[3]Géosciences Environnement Toulouse (GET), Université Paul Sabatier (UPS), Toulouse, France

Commission III, WG III/2

KEY WORDS: GNSS-Reflectometry, CYGNSS, floods detection, coherent reflectivity

ABSTRACT:

This study uses the observations from the Cyclone GNSS (CYGNSS) mission to analyze their potential for a global mapping of the floods dynamics in the pan-tropical area using Global Navigation Satellite System (GNSS) Reflectometry (GNSS-R). We base our analysis on the coherent reflectivity derived from CYGNSS observations. We show that the CYGNSS mission configuration allows a gridding at a spatial resolution of 0.1° (∼11 km at the equator), with a time sampling of 1 week. We calculate the average and standard deviation values of reflectivity in the grid pixels at each time step. A Gaussian weighted window of one month is used to fill the gaps which appear in the time series due to the pseudo-random sampling of CYGNSS observations. The maps of these two parameters are then compared to elevation data from the Shuttle Radar Topography Mission (SRTM) digital elevation model (DEM), to Land Cover information from the European Space Agency's (ESA) Climate Change Initiative (CCI), and to a reference set of static inundation maps. We observe a strong correspondence between CYGNSS reflectivity-based parameters, and the percentage of flooded areas established in the literature. The detection of the major floodplains, irrigated crops, open water areas, and the hydrological network using CYGNSS data is clear. We observe some limitations over the areas with high elevation – due to the CYGNSS mission specificities – and over the most densely vegetated areas. At some point it could prevent the correct extraction of flood patterns. For a future complete CYGNSS-based flood product, the integration of ancillary data describing the major role of land cover, biomass and topography on the GNSS-R returned signals should be necessary to extract the correct features of water cycle.

1. INTRODUCTION

Global Navigation Satellite System (GNSS) Reflectometry (GNSS-R) is one of the emerging tools in remote sensing applied to land surfaces (Zavorotny et al., 2014). It exploits the L-band signals emitted by GNSS satellites and scattered by the Earth's surface, as a bistatic radar configuration where the transmitter and the receiver are separated. The first developments of GNSS-R date back to the early 1990's with some in-situ experiments applied to ocean altimetry (Martin-Neira, 1993). Further applications have included ocean altimetry and winds speed (Anderson, 2000), but also the retrieval of various land surface variables such as soil moisture (Larson et al., 2008, Rodriguez-Alvarez et al., 2011, Roussel et al., 2016), vegetation / biomass (Zhang et al., 2017, Rodriguez-Alvarez et al., 2011), snow and ice cover (Larson et al., 2009), etc. Applications have been first developed as in-situ experiments using either a conventional GNSS-antenna or a dual-antenna configuration. Receivers have been then carried onboard airborne and satellite missions.

The NASA's Cyclone GNSS (CYGNSS) mission was launched in 2016 with the objective to provide a daily, global coverage of winds speed in the pan-tropical area (±38° latitude), in order to monitor the formation and the propagation of tropical cyclones (Ruf et al., 2016). It consists in a constellation of 8 low elevation orbit (LEO) micro-satellites. The Delay Doppler Mapping Instrument (DDMI) onboard every satellite records simultaneously 4 reflected signals each second – 32 in total for the whole constellation. Since the mission was launched, the CYGNSS signals of opportunity collected over land have shown a strong interest for studying land geophysical parameters. The spatial resolution of a coherent scattering over land is estimated to ∼1 x 7 km (Eroglu et al., 2019, Rodriguez-Alvarez et al., 2019, Yan et al., 2020) due to the integration of the signals received from the first Fresnel zone over 1 second, along the satellite track.

Among all the applications of CYGNSS dataset over the land surfaces, soil moisture (SM) has been the most widely studied (Al-Khaldi et al., 2019, Carreno-Luengo et al., 2019, Chew and Small, 2018, Clarizia et al., 2019, Eroglu et al., 2019, Yan et al., 2020). It has been demonstrated that CYGNSS has the ability to monitor the changes in SM content both at the regional and the global scales. Moreover, it can be used to upgrade the spatial and temporal resolution of existing SM products based on Soil Moisture Active Passive (SMAP) and Soil Moisture Ocean Salinity (SMOS) L-band radiometers (Yan et al., 2020). The interaction of GNSS-R signals with the vegetation cover was also studied and the influence of the biomass on the scattered signals is assessed (Carreno-Luengo et al., 2019, Jensen et al., 2018, Rodriguez-Alvarez et al., 2019).

On the wetlands and floods dynamics, no global study has been performed using CYGNSS data. Yet its sensitivity to surface water among other geophysical variables has been assessed (Chew and Small, 2020). Maps of CYGNSS standard deviation of Surface Reflectivity (SR) were used to product a water bodies mask and compare it to the literature (Gerlein-Safdi and Ruf, 2019). Also, various studies performed local or regional

* Corresponding author: pierre.zeiger@legos.obs-mip.fr

comparisons – both spatial or temporal – between flooded and non-flooded areas during cyclones, typhoons, or other natural hazards (Chew et al., 2018, Morris et al., 2019, Wan et al., 2019). However, all these results use a mere threshold, which is highly empirical and only valid at regional scale. The ability to retrieve water extent from CYGNSS data under a dense vegetation canopy layer has also been explored (Jensen et al., 2018, Rodriguez-Alvarez et al., 2019), but these results are still obtained at a regional scale (subset of the Amazon Basin).

We believe that a CYGNSS-derived global flood product would be of high interest due to the characteristics of the mission. In effect, actual wetland monitoring derives either from optical data (Pekel et al., 2016), which is problematic especially in tropical areas – temporal averaging due to clouds, no detection of the inundations below the canopy –, or from active and passive microwave data (Bartsch et al., 2009, Parrens et al., 2017, Prigent et al., 2020). Active radar measurements such as Sythetic Aperture Radar, suffer from a lower temporal repeat (ALOS-1 and 2) and double bounce effect (ENVISAT, RADARSAT-1 and 2, SENTINEL 1) or weak penetration depth (TerraSAR-X) in vegetated areas, while passive microwave measurements operated by radiometers (e.g., SSM/I, AMSR-E, SMAP, SMOS) have spatial resolutions coarser than 20 km. CYGNSS's spatiotemporal resolution could help the understanding of hydrological phenomena in tropical wetlands.

In this paper, we highlight the interest of CYGNSS data for mapping global flood dynamics at a fine spatial and temporal resolution. We show that parameters derived from CYGNSS Delay Doppler Maps (DDM) are sensitive to the presence of water on the reflecting surface. In section 2, we present the different datasets and the processing chain we use to calculate CYGNSS derived parameters. In section 3, we present our results and in section 4, we discuss the conclusions and perspectives to this work.

2. DATA AND METHODS

2.1 CYGNSS reflectivity determination

In this study, we have used the CYGNSS Level 1 version 3.0 files, available in the Physical Oceanography Distributed Active Archive Center (PODAAC: https://podaac.jpl.nasa.gov). We downloaded the power analog Delay Doppler Maps (DDM) along with other useful variables over one year, from August 1st, 2018 to July 31st, 2019. We have extracted the peak of each DDM and applied some quality flags to our dataset, following the literature (Chew and Small, 2018, Eroglu et al., 2019). An ocean mask is also applied to remove non-land points. The CYGNSS reflectivity $\Gamma(\theta)$ is calculated following (Clarizia et al., 2019, Eroglu et al., 2019) assuming a coherent scattering:

$$\Gamma(\theta) = \left(\frac{4\pi}{\lambda}\right)^2 \frac{P_{DDM}(R_r + R_t)^2}{G_r G_t P_t} \quad (1)$$

where λ = 19.03 cm is the GPS L1 wavelength, P_{DDM} is the peak of the DDM analog power, R_r and R_t are the distances from the receiver and the transmitter to the specular point, G_r is the receiver antenna gain, and $G_t P_t$ is the GPS Equivalent Isotopically Radiated Power (EIRP).

Before analyzing this dataset we first grid CYGNSS reflectivity into a 0.1° grid (∼11 km at the Equator). The ideal spatial resolution for a daily CYGNSS product should be larger (∼0.25°) according to our empirical conclusions. Nevertheless, a 0.1° grid can be used to obtain a finer spatial information, with a degraded temporal sampling of 1 week. Some data gaps were also noticed due to the pseudo-random sampling of the CYGNSS observations – explained by the bistatic transmitter-receiver configuration. To avoid a loss of spatial information, a moving window of 30 days with a Gaussian weighting was used to fill the gaps at some time steps. The yearly averaged number of observations used to grid CYGNSS observations is plotted in Figure 1. We notice that it is higher in the tropics due to the orbit of CYGNSS mission, and lower around the equator. This is of course a constraint for the mapping of floods in these regions, including Amazon, Orinoco and also Congo basins.

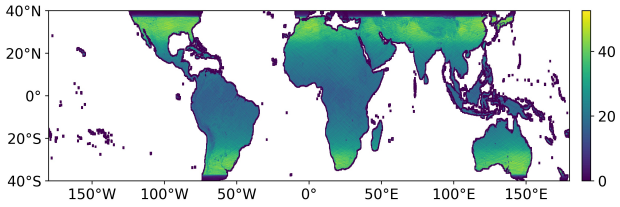

Figure 1. Mean number of CYGNSS observations in time in the 0.1° grid. Colour scale ranges from dark blue (zero) to yellow (maximum of ∼40 observations per cell in the tropics)

The weighted average and standard deviation values of CYGNSS reflectivity in this moving window for every pixel are used to fill the grid's time steps. They are respectively noted Γ_{mean} and Γ_{std}. This results in a weekly 0.1° (∼11 km) grid of two parameters that describe the average level of reflectivity and the dispersion or heterogeneity in a pixel at each time step. Figure 2 presents the spatial patterns of yearly averaged values of Γ_{mean} and Γ_{std} per pixel. These variables are used for further analysis along with some ancillary data in section 3.

2.2 Description of the ancillary data

To compare with CYGNSS reflectivity, we use 3 different types of data. First, static inundation maps are used to assess the link between CYGNSS parameters – Γ_{mean} and Γ_{std} – and the reference level of flood occurrence in the pixel. Then, land cover maps are used to evaluate the response of CYGNSS reflectivity depending on the type of soil and vegetation. Finally, we also use a Digital Elevation Model (DEM) to further evaluate the dependence of CYGNSS recorded signals to the elevation.

We used for flood estimation the static wetland maps at 15" (∼500 m at the Equator), from (Tootchi et al., 2019). It combines both maps of the Regularly Flooded Wetlands (RFW) – coming from various inundation datasets – and of the Groudwater Wetlands modeling (GDW) into a single dataset, called Composite Wetlands (CW). In theory CYGNSS observations should be sensitive to the floods whatever their origin is – river discharge and precipitations, or groundwater. However, it appears that CW maps are saturated and show floods even in non-wet regions of Sahel, probably due to an overestimation of the influence of groundwaters. Thus we have only used RFW maps for further analysis.

For Land Cover (LC) information, we use the European Space Agency's (ESA) Climate Change Initiative (CCI) global LC maps at 300 m resolution (ESA, 2017). They are obtained from 1992 to 2015 combining different imagery products including the reflectance time series from Medium Resolution Imaging

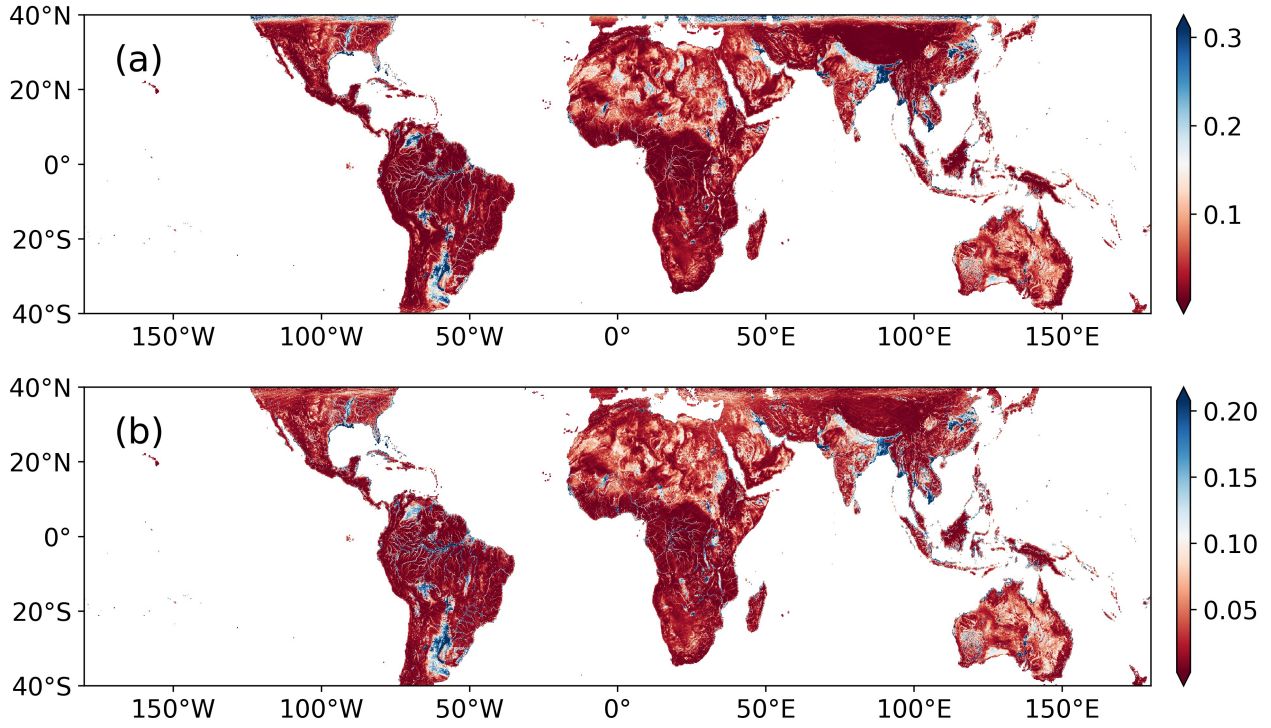

Figure 2. Mean annual value of: **(a)** Γ_{mean}, **(b)** Γ_{std}. High values corresponding to water objects are shown in blue.

Spectrometer (MERIS). These maps are based on the GlobCover unsupervised classification algorithm (Defourny et al., 2007), and further extended from 2016 to 2019 by the Copernicus Climate Change Service (C3S). In this study we use the 2019 LC map which fits better our time series. The CCI LC Classification System (LCCS) used is composed of 38 classes. No table of the LC classes is provided in this paper, but readers are invited to visit the CCI website or to download metadata from the CCI LC project. For further analysis, only the codes corresponding to each LC type and the colors associated to each class in CCI LC metadata are shown.

The DEM used is the Shuttle Radar Topography Mission Global 1-km DEM (SRTM30+) Version 11 for land surfaces, which is distributed by the Pacific Islands Ocean Observing System (PacIOOS) (Sandwell et al., 2014).

All the ancillary data are regridded to our CYGNSS 0.1° grid for better comparison and for minimizing scale effects. For static flood maps, the percentage of water in each pixel is computed. For CCI LC, the percentage of each type of land cover in the pixels is extracted. This allow us to identify the dominant LC type. For the DEM, the mean and the standard deviation of the elevation – which is a proxy for the slope – are extracted in each grid cell.

3. EVALUATION OF CYGNSS REFLECTIVITY FOR FLOOD DETECTION

3.1 Empirical Orthogonal Functions of CYGNSS reflectivity

We have performed an Empirical Orthogonal Functions (EOFs) analysis over the one year time series of Γ_{mean} and Γ_{std}, in order to extract the spatial and temporal patterns of CYGNSS reflectivity. EOFs maps for the first 5 modes are shown in Figure 3 along with the time series of the principal components (PC) associated. The addition of the first five modes explain $\sim$72% of the total variance.

The time series of PC1 and PC2 (see Figure 3.a2 and 3.b2) show a well-marked seasonal variation with a maximum during the spring (PC1) and the late summer (PC2), respectively. We notice in EOF1 and EOF2 maps (Figure 3.a1 and 3.b1) that this climatology mainly corresponds to the changes in reflectivity in regions affected by floods and high SM content. The first mode phase in the water cycle between the northern hemisphere in blue (Orinoco, Niger, Chad, Ganges, Mekong rivers) and the southern hemisphere in red (most of the Amazon basin, La Plata Basin, south of Africa, Australia). Notable exceptions are Mississippi and Yangtze rivers that show maximums concordant with the southern hemisphere. The second mode shows some residuals and a separation between permanent water and seasonal water or SM, mainly visible in the Sahel region.

The modes number 3, 4 and 5 correspond to EOF maps in Figure 3.c1, d1, e1 and PC time series in Figure 3.c2, d2, e2 respectively. They show a maximum of 10% variance explained with a bimodal time series during the year. This corresponds to residuals or local climatologies differing from global patterns at the scale of the watersheds. The further modes (not shown in Figure 3) with smaller variance explained and higher variability throughout the year, are more sensitive to noise. We can still conclude that for modes n°1 to, 5, the main spatial patterns observed correspond to regions severely affected by seasonal floods, permanent water or irrigated croplands.

3.2 Comparison with ancillary data

A regional comparison between CYGNSS reflectivity (in the left panel) and other data – inundation maps from (Tootchi et al., 2019) in the center panel, CCI LC maps in the right panel

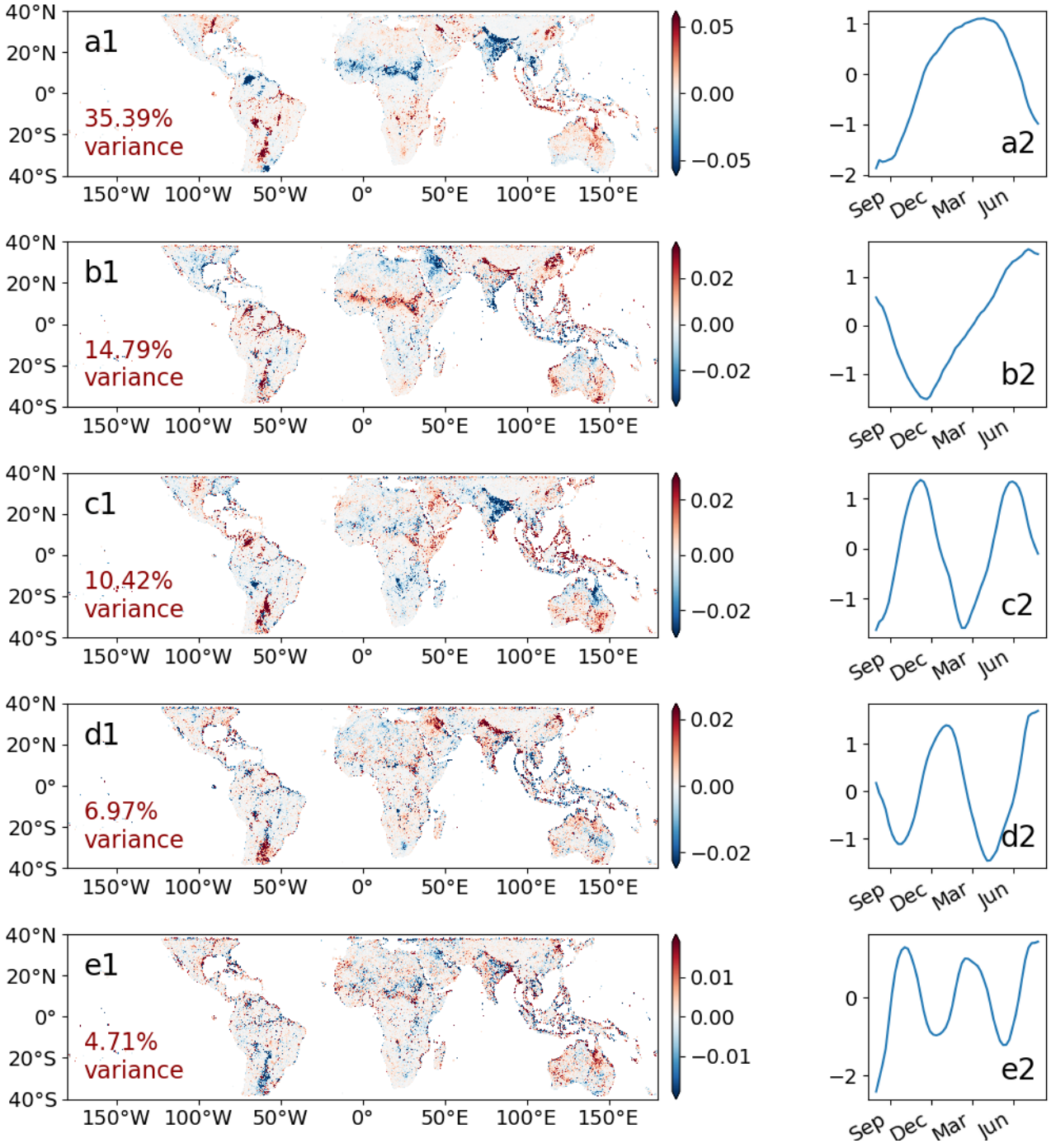

Figure 3. First 5 modes of the Empirical Orthogonal Functions applied to Γ_{mean}. The explained variance ratio for each mode is printed in bottom left corner of the maps. **(a1)**, **(b1)**, **(c1)**, **(d1)**, **(e1)** show the map of covariance between Γ_{mean} and the principal components (PC) for modes n°1, 2, 3, 4, 5 respectively. **(a2)**, **(b2)**, **(c2)**, **(d2)**, **(e2)** show the time series of the PC for the same modes.

– is shown in Figure 4. Figure 4.a1-3 shows these parameters over South America, Figure 4.b1-3 over central Africa, and Figure 4.c1-3 over India and the Himalayas. First, we note that the great floodplains located in South America such as the central Orinoco Basin, the central and southern parts of the La Plata Basin and Llanos de Mojos - in the southwest of the Amazon Basin - (Figure 4.a1, a2), as well as inundations and irrigated crops in India (Figure 4.c1, c2) and various lakes, reservoirs and wetlands such as lake Chad and the Inner Niger Delta (Figure 4.b1, b2) exhibit high values of Γ_{std}. In all these cases, the CYGNSS reflectivity fits well with the reference inundation maps. If we take a look at the LC information, we notice that all these areas are covered by either a non-dense tree cover or a low vegetation layer such as shrubs, herbaceous and crops. On the contrary, some floodplains under a very dense tree layer in equatorial forests are not correctly monitored by CYGNSS, especially for the Cuvette Central of Congo (Figure 4.a2).

We have also computed the spatial correlation coefficient between CYGNSS parameters and the reference static flood maps for the main river basins in these regions. The maximum spatial correlation at the scale of the watershed is obtained dur-

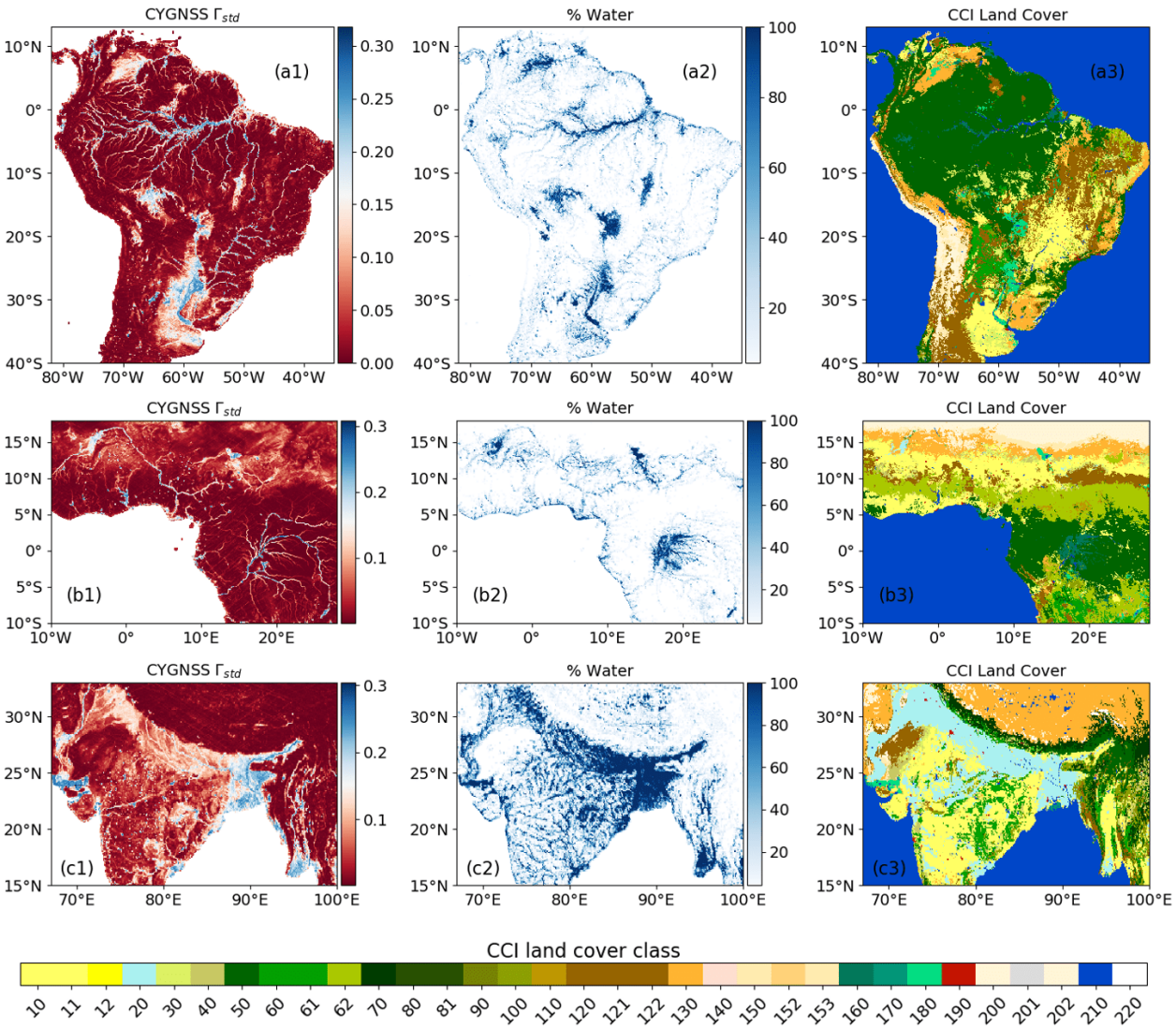

Figure 4. Comparison of CYGNSS mean reflectivity with Tootchi's inundation maps and CCI Land Cover classification. **(a1)**, **(a2)**, **(a3)** show respectively an average of Γ_{std} over the year, the maximal percentage of floods in each pixel, and the dominant LC type in the pixel over South America. Orinoco, Amazon and La Plata floodplains are highly visible in blue. **(b1)**, **(b2)** and **(b3)** show the same variables plotted over the Sahel and Congo region, including the Niger and a part of the Congo basins. **(c1)**, **(c2)** and **(c3)** show the same variables over the eastern part of India, where the seasonal floods and the irrigation of croplands in the Ganges-Brahmaputra basin is frequent. For more information about the CCI LC classes, readers are invited to visit the CCI webpage

ing flood events, and shown in Table 1. For Amazon, Orinoco, La Plata and Ganges basins, we obtain a correlation greater than 0.74 using Γ_{mean}. This confirms that CYGNSS is able to monitor the major floodplains in the pan-tropical area. Lower correlation values are obtain for Niger and Congo basins. We attribute it to the influence of dense vegetation layers in Congo, and to arid soils producing a strong reflection (thus a saturation of the signal) in Niger.

The maps of Γ_{std} in South America and Central Africa show a good delineation of the hydrological network when the rivers reach a minimum width. This is highly visible in the Amazon and Congo basins. This is due to the mixing of reflections over open water and riverbanks in the same CYGNSS pixels, producing a high value of Γ_{std}. However, the dense tree canopy out of the water bodies in these regions drastically reduces the penetration of L-band signals (Parrens et al., 2017). This affects a potential mapping of floods in equatorial forests using

Table 1. Spatial correlation coefficients computed between Tootchi's RFW map and CYGNSS Γ_{mean} and Γ_{std} for the main river basins visible in Figure 4.

Basin	**Spatial correlation**	
	RFW vs Γ_{mean}	**RFW vs Γ_{mean}**
Amazon	0.77	0.69
Orinoco	0.75	0.68
Parana / La Plata	0.74	0.67
Niger	0.49	0.48
Congo	0.58	0.58
Ganges / Brahm.	0.76	0.74

CYGNSS, as it is confirmed with the example of the Cuvette Centrale of Congo. This is a global limitation for all inundation products based on microwave data, while the optical sensors perform even worse in equatorial forests due to the frequent

cloud cover and the canopy layers.

Finally, the example of India in Figure 4.c1-3 show a strong detection of the inundated or irrigated croplands (LC class n°20 in cyan) in the Ganges-Brahmaputra basin. All under the Himalayan arc, Γ_{std} has medium to high values with an important variability throughout the year. These areas fit well to pixels with a high percentage of floods during the year (Figure 4.c2) and whose land cover is dominated by irrigated croplands (Figure 4.c3).

All these results highlight the high potential of CYGNSS for mapping the presence of permanent or seasonal water in the pan-tropical area. A limitation is observed in some dense vegetated areas when comparing to LC information.

4. DISCUSSION

Some factors limit the ability of CYGNSS to correctly monitor floods and permanent water and should be discussed. It is commonly known that a dense vegetation layer reduces the penetration of GPS signals in equatorial forests, and so the reflectivity of CYGNSS observations. This is particularly visible in the Congo basin, where floodplains play an important role in the storage of fresh water during seasonal floods, regulating the flow of the river for natural needs and human activities. Researches are still in progress to overcome this problem for radar-based flood products, as optical data are non-adapted when the vegetation is dense.

The topography – and particularly the elevation higher than 600 m – has also a strong influence on CYGNSS reflectivity. This is due to the onboard CYGNSS mission algorithms for the estimation of the specular point localization, which are based on the geoid. As the mission is designed for ocean applications, the problem has appeared when trying to use CYGNSS data over land. Some studies apply an elevation mask over 600 m to remove a source of uncertainty. However, this removes ∼35% of the total CYGNSS pixels in our case, and these areas still contain valuable information. An example for the Titicaca Lake is shown in Figure 5.c and below.

Figure 5 show the annual mean reflectivity value for lake pixels (Figure 5.a) and flood pixels (Figure 5.b). In both cases, we observe a strong decrease of Γ_{mean} when the elevation increases. In fact, the heterogeneity of CYGNSS observations over water pixels is high, with a yearly mean Γ_{mean} value ranging from 0 to ∼0.65 (at particular time steps, the dynamic range is from 0 to 1). On the contrary, for elevations above ∼2 km, Γ_{mean} is generally lower than 0.2.

In Figure 5.c we can see a map of CYGNSS mean reflectivity over the Titicaca Lake, which is ∼3800 m high. Typically, the Γ_{mean} values are lower than 0.2. However, we notice a good delineation of the Titicaca Lake coastline while reflectivity values are close to 0 over non-inundated areas. This illustrates why we prefer not to filter out high elevation pixels, as they contain a valuable information. The risk in those cases is to create a confusion between high elevation, water pixels and low elevation, non-wet pixels affected by roughness, topography, etc. As an example, some pixels over bare soils in the Sahara and in Arabian Peninsula show a ∼constant time series of reflectivity with a medium amplitude, which is the same pattern observed over the Titicaca Lake. A complete CYGNSS-based floods and water pixels retrieval would require some ancillary data to overcome this problem. These data should be, in our opinion, at least composed of a DEM and a Land Cover classification, as CYGNSS recorded signals are affected by both the elevation and the type of vegetation layers in the reflecting surface. Additional information could also be extracted from the DEM – as the slope or RMS of elevation – as well as from other sources of data. An information of biomass content or L-band Vegetation Optical Depth (L-VOD) (Wigneron et al., 2021) can be helpful in this process.

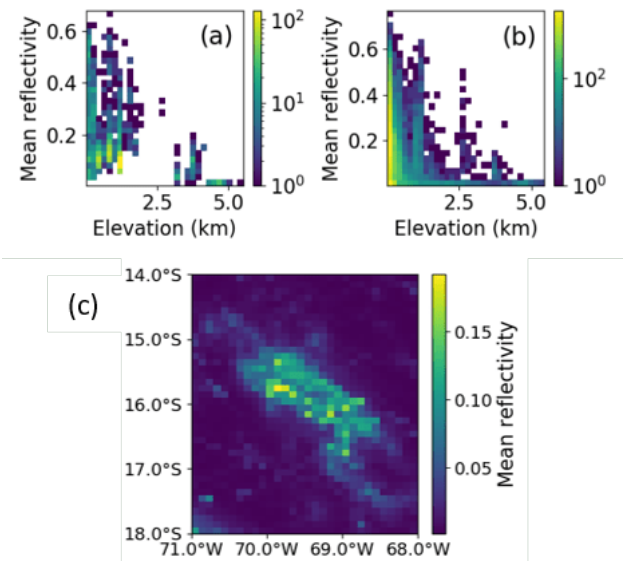

Figure 5. Density plots of CYGNSS reflectivity vs the elevation. **(a)** Pixels over lakes, **(b)** pixels over floodplains, and **(c)** map of CYGNSS mean reflectivity over the Titicaca Lake at 3800 m high.

5. CONCLUSION

In this study, we have analyzed the mean and standard deviation values of reflectivity – noted Γ_{mean} and Γ_{std} respectively – gridded on a 0.1°, 7 days grid over the entire CYGNSS mission coverage. The objective of our study is to assess the interest of CYGNSS for mapping flood dynamics at a global scale, with an improved spatiotemporal resolution when compared to existing products such as GIEMS. Our results suggest that CYGNSS observations are highly sensitive to the content of water in the grid pixels. The first modes of an EOF decomposition are dominated by annual variations of the reflectivity over some areas severely flooded or with a high soil moisture climatology over the year. Some local patterns are then identified and explain a lower quantity of variance. Maps of CYGNSS Γ_{mean} and Γ_{std} compared to static inundation maps suggest that the main floodplains and open water areas are correctly identified in these parameters.

We have identified two main limitations for a CYGNSS-based flood product. First, the L-band GPS signals are partially filtered out by vegetation layers over the deepest equatorial forests, especially in the Cuvette Central of Congo. This problem is common to microwave remote sensing observations. Then, the elevation is a key factor as CYGNSS specular point estimation is based on geoid. We show that while the mean reflectivity decreases with the altitude, it still contains valuable information over the lakes and floodplains at high elevation.

These observations open the track to the evaluation of a

This contribution has been peer-reviewed. The double-blind peer-review was conducted on the basis of the full paper.
https://doi.org/10.5194/isprs-annals-V-3-2022-93-2022 | © Author(s) 2022. CC BY 4.0 License.

CYGNSS-based, pan-tropical floods product. It would require additional information from topography, land cover and biomass to overcome the limitations observed in this paper. Such a product would still be of high interest for the hydrological community, as it should be able to retrieve the inundation extent on a 0.1°, 7 days spatial and temporal resolution basis. It would be a valuable complement to GIEMS (Prigent et al., 2020) or other Earth observation products whose resolution, either spatial or temporal, is much lower. A comparable process has been developed for SM estimation, where CYGNSS is able to fill the gaps in existing products from microwave radiometers.

REFERENCES

Al-Khaldi, M. M., Johnson, J. T., O'Brien, A. J., Balenzano, A., Mattia, F., 2019. Time-Series Retrieval of Soil Moisture Using CYGNSS. *IEEE Trans. Geosci. Remote Sensing*, 57(7), 10.

Anderson, K. D., 2000. Determination of Water Level and Tides Using Interferometric Observations of GPS Signals. *Journal of Atmospheric and Oceanic Technology*, 17(8), 1118 - 1127. https://journals.ametsoc.org/view/journals/atot/17/8/1520-$0426_2000_017_1118_dowlat_2.0.co_2.xml$.

Bartsch, A., Wagner, W., Scipal, K., Pathe, C., Sabel, D., Wolski, P., 2009. Global monitoring of wetlands – the value of ENVISAT ASAR Global mode. *Journal of Environmental Management*, 90(7), 2226–2233.

Carreno-Luengo, H., Luzi, G., Crosetto, M., 2019. Sensitivity of CyGNSS Bistatic Reflectivity and SMAP Microwave Radiometry Brightness Temperature to Geophysical Parameters over Land Surfaces. *IEEE J. Sel. Top. Appl. Earth Observations Remote Sensing*, 12(1), 107–122. Publisher: IEEE.

Chew, C. C., Small, E. E., 2018. Soil Moisture Sensing Using Spaceborne GNSS Reflections: Comparison of CYGNSS Reflectivity to SMAP Soil Moisture. *Geophysical Research Letters*, 45(9), 4049–4057.

Chew, C., Reager, J. T., Small, E., 2018. CYGNSS data map flood inundation during the 2017 Atlantic hurricane season. *Sci Rep*, 8(1), 9336.

Chew, C., Small, E., 2020. Estimating inundation extent using CYGNSS data: A conceptual modeling study. *Remote Sensing of Environment*, 246, 111869.

Clarizia, M. P., Pierdicca, N., Costantini, F., Floury, N., 2019. Analysis of CYGNSS Data for Soil Moisture Retrieval. *IEEE J. Sel. Top. Appl. Earth Observations Remote Sensing*, 12(7), 9.

Defourny, P., Vancutsem, C., Bicheron, P., Brockmann, C., Nino, F., Schouten, L., Leroy, M., 2007. GlobCover: A 300M Global Land Cover Product for 2005 Using ENVISAT MERIS Time Series. *Proceedings of the ISPRS Commission VII Symposium Remote Sensing: From Pixels to Processes*, Enschede, The Netherlands, 4.

Eroglu, O., Kurum, M., Boyd, D., Gurbuz, A. C., 2019. High spatio-temporal resolution cygnss soil moisture estimates using artificial neural networks. *Remote Sensing*, 11(19).

Gerlein-Safdi, C., Ruf, C. S., 2019. A CYGNSS-Based Algorithm for the Detection of Inland Waterbodies. *Geophysical Research Letters*, 46(21), 12065–12072.

Jensen, K., McDonald, K., Podest, E., Rodriguez-Alvarez, N., Horna, V., Steiner, N., 2018. Assessing L-Band GNSS-reflectometry and imaging radar for detecting sub-canopy inundation dynamics in a tropicalwetlands complex. *Remote Sensing*, 10(9).

Larson, K. M., Gutmann, E. D., Zavorotny, V. U., Braun, J. J., Williams, M. W., Nievinski, F. G., 2009. Can we measure snow depth with GPS receivers? *Geophysical Research Letters*, 36(17), 1–5.

Larson, K. M., Small, E. E., Gutmann, E. D., Bilich, A. L., Braun, J. J., Zavorotny, V. U., 2008. Use of GPS receivers as a soil moisture network for water cycle studies. *Geophysical Research Letters*, 35(24), 1–5.

Martin-Neira, M., 1993. *A passive reflectometry and interferometry system (PARIS): application to ocean altimetry*. 17Number 4. ISSN: 03792285 Publication Title: ESA Journal.

Morris, M., Chew, C., Reager, J. T., Shah, R., Zuffada, C., 2019. A novel approach to monitoring wetland dynamics using CYGNSS: Everglades case study. *Remote Sensing of Environment*, 233, 111417.

Parrens, M., Al Bitar, A., Frappart, F., Papa, F., Calmant, S., Crétaux, J.-F., Wigneron, J.-P., Kerr, Y., 2017. Mapping Dynamic Water Fraction under the Tropical Rain Forests of the Amazonian Basin from SMOS Brightness Temperatures. *Water*, 9(5), 350.

Pekel, J.-F., Cottam, A., Gorelick, N., Belward, A. S., 2016. High-resolution mapping of global surface water and its long-term changes. *Nature*, 540(7633), 418–422.

Prigent, C., Jimenez, C., Bousquet, P., 2020. Satellite-Derived Global Surface Water Extent and Dynamics Over the Last 25 Years (GIEMS-2). *J. Geophys. Res. Atmos.*, 125(3).

Rodriguez-Alvarez, N., Camps, A., Vall-Llossera, M., Bosch-Lluis, X., Monerris, A., Ramos-Perez, I., Valencia, E., Martinez-Fernandez, J., Baroncini-Turricchia, G., Perez-Gutierrez, C., Sanchez, N., Marchan-Hernandez, J. F., 2011. Land geophysical parameters retrieval using the interference pattern GNSS-R technique. *IEEE Trans. Geosci. Remote Sensing*, 49(1 PART 1), 71–84.

Rodriguez-Alvarez, N., Podest, E., Jensen, K., McDonald, K. C., 2019. Classifying Inundation in a Tropical Wetlands Complex with GNSS-R. *Remote Sensing*, 11(9), 1053.

Roussel, N., Frappart, F., Ramillien, G., Darrozes, J., Baup, F., Lestarquit, L., Ha, M. C., 2016. Detection of Soil Moisture Variations Using GPS and GLONASS SNR Data for Elevation Angles Ranging From 2° to 70°. *IEEE J. Sel. Top. Appl. Earth Observations Remote Sensing*, 9(10), 4781–4794. http://ieeexplore.ieee.org/document/7446285/.

Ruf, C. S., Atlas, R., Chang, P. S., Clarizia, M. P., Garrison, J. L., Gleason, S., Katzberg, S. J., Jelenak, Z., Johnson, J. T., Majumdar, S. J., O'Brien, A., Posselt, D. J., Ridley, A. J., Rose, R. J., Zavorotny, V. U., 2016. New ocean winds satellite mission to probe hurricanes and tropical convection. *Bulletin of the American Meteorological Society*, 97(3), 385–395.

Sandwell, D., Smith, W., Becker, J., 2014. SRTM30+ global 1-km Digital Elevation Model (DEM): Version 11: Land surface, distributed by the Pacific Islands Ocean Observing System (PacIOOS). Accessed: 2021-11-18.

Tootchi, A., Jost, A., Ducharne, A., 2019. Multi-source global wetland maps combining surface water imagery and groundwater constraints. *Earth Syst. Sci. Data*, 11, 189-220.

Wan, W., Liu, B., Zeng, Z., Chen, X., Wu, G., Xu, L., Chen, X., Hong, Y., 2019. Using CYGNSS Data to Monitor China's Flood Inundation during Typhoon and Extreme Precipitation Events in 2017. *Remote Sensing*, 11(7), 854.

Wigneron, J.-P., Li, X., Frappart, F., Fan, L., Al-Yaari, A., De Lannoy, G., Liu, X., Wang, M., Le Masson, E., Moisy, C., 2021. SMOS-IC data record of soil moisture and L-VOD: Historical development, applications and perspectives. *Remote Sensing of Environment*, 20.

Yan, Q., Huang, W., Jin, S., Jia, Y., 2020. Pan-tropical soil moisture mapping based on a three-layer model from CYGNSS GNSS-R data. *Remote Sensing of Environment*, 247, 111944.

Zavorotny, V. U., Gleason, S., Cardellach, E., Camps, A., 2014. Tutorial on remote sensing using GNSS bistatic radar of opportunity. *IEEE Geoscience and Remote Sensing Magazine*, 2(4), 8–45. Publisher: IEEE.

Zhang, S., Roussel, N., Boniface, K., Cuong Ha, M., Frappart, F., Darrozes, J., Baup, F., Calvet, J. C., 2017. Use of reflected GNSS SNR data to retrieve either soil moisture or vegetation height from a wheat crop. *Hydrology and Earth System Sciences*, 21(9), 4767–4784. ISBN: 2147672017.